

Optical Engineering

SPIDigitalLibrary.org/oe

Hyperspectral microscopy of explosives particles using an external cavity quantum cascade laser

Mark C. Phillips
Bruce E. Bernacki

Hyperspectral microscopy of explosives particles using an external cavity quantum cascade laser

Mark C. Phillips

Bruce E. Bernacki

Pacific Northwest National Laboratory

P.O. Box 999

Richland, Washington 99352

E-mail: mark.phillips@pnnl.gov

Abstract. Using infrared hyperspectral imaging, microscopy of small particles of the explosives compounds RDX, tetryl, and PETN with near diffraction-limited performance is demonstrated. The custom microscope apparatus includes an external cavity quantum cascade laser illuminator scanned over its tuning range of 9.13 to 10.53 μm in 4 s, coupled with a microbolometer focal plane array to record infrared transmission images. The hyperspectral microscopy technique is used to study the infrared absorption spectra of individual explosives particles, and demonstrate subnanogram detection limits. © The Authors. Published by SPIE under a Creative Commons Attribution 3.0 Unported License. Distribution or reproduction of this work in whole or in part requires full attribution of the original publication, including its DOI. [DOI: [10.1117/1.OE.52.6.061302](https://doi.org/10.1117/1.OE.52.6.061302)]

Subject terms: infrared spectroscopy; quantum cascade laser; tunable laser; infrared microscopy; explosives detection.

Paper 121311SSP received Sep. 11, 2012; revised manuscript received Oct. 23, 2012; accepted for publication Nov. 8, 2012; published online Dec. 26, 2012.

1 Introduction

Hyperspectral imaging using broadly tunable external cavity quantum cascade lasers (ECQCLs) offers the potential for high-speed chemical imaging of gas, liquid, and solid compounds over a wide range of magnifications. Operating in the mid-infrared (MIR) “fingerprint” spectral region of 3 to 25 μm , ECQCLs provide a high-brightness tunable laser source for infrared spectroscopy and imaging. We have previously demonstrated hyperspectral imaging using ECQCL illumination in both transmission and reflection geometries; however, the spatial resolution of these systems was limited as they were designed for imaging large fields-of-view.^{1,2} We have recently adapted these hyperspectral imaging techniques to microscopy applications, in which the infrared absorption spectra of small particles or spatial features can be studied.³

Microscopic chemical imaging in the MIR spectral region is often performed using Fourier-transform infrared (FTIR) spectroscopy techniques.⁴⁻⁶ However, the low spectral radiance of the broadband thermal illumination source places limitations on this technique. As a result, acquiring high signal-to-noise ratio (SNR) images demands long data acquisition times, especially when high magnification or high spectral resolution is desired. Many of the limitations can be overcome using synchrotron radiation sources to provide a higher spectral radiance,⁷⁻⁹ but these systems can have a high cost and low availability.

Laser sources in the MIR provide a high spectral radiance and coherent beam well suited to microscopy applications,¹⁰ but have often been limited by a lack of wavelength tuning range. The quantum cascade (QC) laser has emerged as a high performance semiconductor laser for MIR spectroscopy, offering high output power and high spectral radiance in a compact and robust device.¹¹ Early uses of QC lasers in microscopic chemical imaging capitalized on their high brightness,¹² but were limited by a small wavelength tuning range. The ECQCL source overcomes this limitation by providing a tuning range of 10% to 20% of its center wavelength or greater.¹³ The high spectral

brightness enables fast acquisition of hyperspectral images at a large number of spectral bands, and allows use of a low-cost uncooled microbolometer focal plane array (FPA) detector² instead of a cryogenically cooled HgCdTe (MCT) detector. While this manuscript presents results from using ECQCLs in far-field microscopy, recent studies are applying ECQCLs to near-field microscopy techniques, allowing combined spectroscopy and imaging on nanometer length scales.^{14,15}

Development of new techniques for rapid detection and identification of explosives is currently an area of high interest and need.^{16,17} Standoff or noncontact techniques are often required for in-field detection when physical sampling is undesirable due to safety concerns, access limitations, need to preserve sample integrity, or slow speed of laboratory analysis. Optical techniques have many advantages for non-contact detection of solids including explosives, using light to interact with a sample and propagate spectral information potentially over long distances. Techniques using MIR light in particular show great promise for standoff explosives detection due to the richness of spectral information and high absorption cross sections in the MIR. Many investigations using QC laser illumination for standoff detection of explosives have been reported.^{1,18-21} However, interpretation of the detected spectra from solid materials including explosives is challenging for relevant samples, increasing the difficulty of reliable threat detection.²² For the case of detecting explosives particles or residues on a surface, the observed spectrum can include effects not only from the material composition, but also from effects such as sample morphology, particle density, or observation geometry. Because standoff techniques at large distances are limited in spatial resolution, the observed spectra are typically averages over multiple particles or regions of a residue. To help understand the fundamental spectroscopy of the individual small particles, we are motivated to apply microscopic spectroscopy techniques to the problem of explosives detection. Understanding the spectroscopy of small particles will provide insight into the spectra resulting from observation of a collection of particles.

For example, plastic-bonded explosives C-4 and Semtex contain particles of cyclotrimethylenetrinitramine (RDX) and/or pentaerythritol tetranitrate (PETN) in a matrix of binders, and a range of particle sizes may be present in residues from fingerprints.²³ The work presented in this paper shows that small nanogram-scale particles of explosives can be imaged with spatially resolved infrared transmission spectra, providing a first step toward these fundamental spectroscopic investigations. In addition, the work demonstrates that sub-nanogram detection limits for explosives particles are possible, which may have applications for trace detection of explosives and other materials.

In this paper, we describe a custom apparatus used for microscopic hyperspectral imaging of explosives particles and residues. An ECQCL operating in the 9.13 to 10.53 μm wavelength range was coupled with an infrared FPA and infrared optics to allow imaging with near diffraction-limited performance. The combination of a tunable infrared laser and an FPA detector allows rapid data acquisition with high SNR. By tuning the ECQCL illumination wavelength and acquiring a hypercube consisting of images at each wavelength, we measure the infrared transmission spectrum of explosives particles, and use this information for identification and characterization. Absorption spectra of explosives particles with nanogram to subnanogram mass are measured. We present an example of a matched filter analysis of hyperspectral images for material identification based on infrared absorption spectra. A noise characterization of the system is performed and used to predict system performance for general materials with infrared absorption. While we have applied the hyperspectral microscopy system to measure explosives particles, the apparatus could be used to study a wide range of materials with applications in materials science, solid-state spectroscopy, and biology.

2 Experimental Setup

Figure 1(a) shows a schematic of the imaging setup used in these experiments. The setup provided transmission microscopy of particles in the sample plane, with imaging provided by an infrared FPA. The FPA detection allows for high-speed image acquisition, which is beneficial in hyperspectral imaging applications where images must be acquired at different wavelengths. To provide active illumination of the samples, an ECQCL designed and constructed in our laboratory was used. The ECQCL design and general performance has been reported previously,²⁴ so here we only present the relevant features for this study. The QC laser device was designed to emit at a center wavelength of 9.75 μm . The device had an antireflection coating on the front facet and a high-reflection coating on the back facet. Current was supplied to the QC laser using a custom current controller providing a sinusoidal waveform at 100 kHz frequency with 0 to 1100 mA current. The QC device was held at 15°C using a thermoelectric cooler, and was placed into a Littman-Metcalf external cavity configuration, which provided wavelength selection and tuning through a galvanometer-mounted tuning mirror.

The ECQCL provided a tuning range of 950 to 1095 cm^{-1} (9.13 to 10.53 μm), with average powers up to 5 mW, as shown in Fig. 1(b). The ECQCL could be scanned over its entire tuning range in less than 50 ms if desired; however, for the studies presented here it was scanned over its tuning range in 4 s, limited by the frame rate of the FPA. Wavelength calibration was performed by transmitting the ECQCL beam through a gas cell containing methanol and matching the observed absorption peaks to those in the Northwest Infrared (NWIR) spectral library.²⁵ The collimated ECQCL output beam had a $1/e^2$ diameter of 3.5 mm; however, propagation over the 2 m distance to the sample

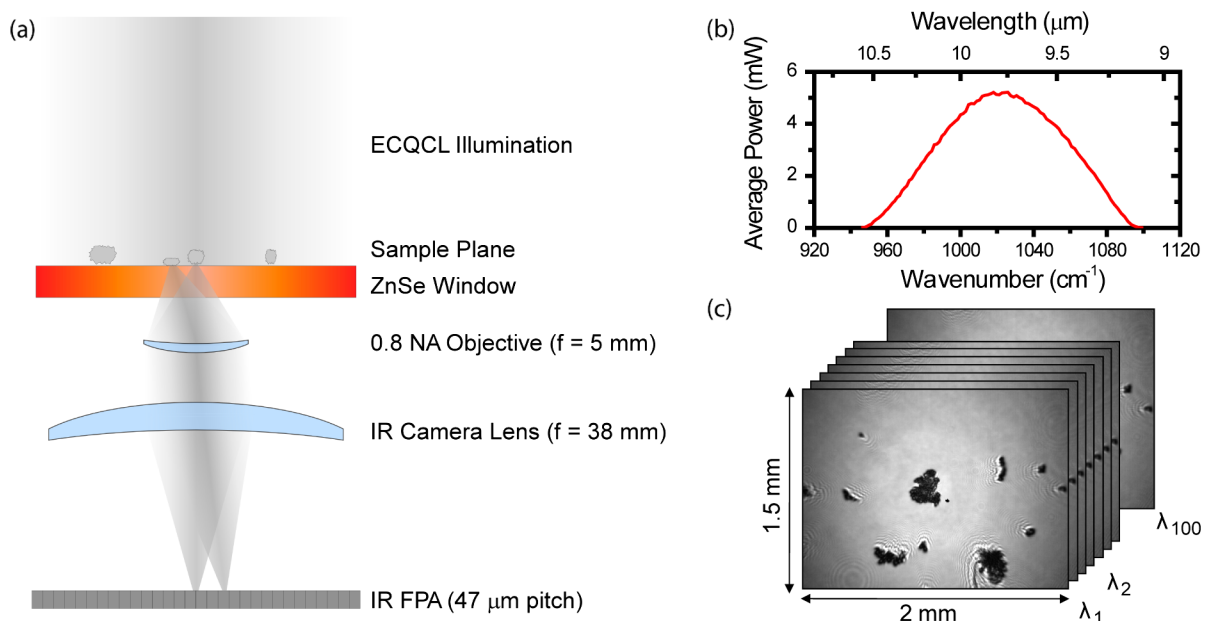


Fig. 1 Experimental setup. (a) Schematic of transmission microscope apparatus. The ECQCL beam is transmitted through the sample plane, which is imaged onto the infrared focal plane array (FPA) using a 0.8 NA objective lens and the IR camera lens. (b) Output average power versus wavelength for the ECQCL. (c) Representation of an image hypercube with 100 images acquired at different wavelength bands. The image corresponds to a 2 mm \times 1.5 mm region of the sample plane.

increased the beam diameter significantly. Therefore, to increase the illumination intensity at the sample, an additional 2 in. diameter 100 mm focal length lens was inserted into the ECQCL beam path. The distance from this lens to the sample was adjusted to provide high illumination intensity at the sample without saturating the FPA detector. Note that an optimized system could be made more compact than the demonstration system presented here.

The thermal infrared camera (FLIR Thermovision A40) used an uncooled microbolometer FPA with 320×240 pixels. Digital 16-bit images were acquired at a rate of 25 Hz, synchronized with the tuning of the ECQCL. For the studies here, the four-second acquisition time provided a hypercube with 100 wavelength bands separated by approximately 1.5 cm^{-1} (15 nm). Figure 1(c) shows a graphical representation of an image hypercube acquired by the system. Each hypercube consists of 100 images acquired at different illumination wavelengths; equivalently, each image pixel contains the sample transmission at each of the 100 sampled wavelengths. For diagnostic purposes including background subtraction of the ambient thermal radiation, images were acquired for wavelengths outside the ECQCL tuning range, for which no light was emitted from the ECQCL. For image spectral analysis only the central 90 wavelength bands were used, corresponding to a spectral range from 953 to 1090 cm^{-1} (9.17 to $10.49 \mu\text{m}$). The hyperspectral image acquisition parameters were selected to provide a compromise between acquisition speed and spectral resolution. If desired, the scan speed of the ECQCL could be adjusted for faster acquisition at lower spectral resolution, or for a slower scan at higher spectral resolution. In addition, a subset of the tuning range could be selected to further reduce the hyperspectral image acquisition time.

Samples were placed on either 1 in. diameter or 0.5 in. diameter ZnSe windows with antireflection coatings. The ECQCL beam was transmitted through the window and samples. An optical system was constructed to image the samples using a custom 0.5 in. diameter 0.8 NA Ge aspheric lens (5 mm effective focal length), combined with the 50 mm diameter, 38 mm focal length lens of the FLIR camera, which provided a calculated magnification of 7.6. The image scale was calibrated by imaging an object of known dimensions, from which a scale factor of $6.4 \mu\text{m}/\text{pixel}$ was determined. Using the FPA pixel pitch of $47 \mu\text{m}$, the experimentally determined magnification was 7.5 in good agreement with the value calculated from the lens focal lengths. The imaged sample region had dimensions $2 \text{ mm} \times 1.5 \text{ mm}$, as indicated in Fig. 1(c). The edge response (10% to 90%) was measured to be $13 \mu\text{m}$, corresponding to two pixels and demonstrating near-diffraction limited imaging. Over the ECQCL wavelength tuning range, the calculated diffraction limited spot size for the 0.8 NA objective lens ranges from 7 to $8 \mu\text{m}$.

The explosives samples were obtained in the form of standard solutions from AccuStandard consisting of RDX, tetryl, and PETN dissolved in acetonitrile and/or methanol with 1 mg/mL concentrations. While readily available and convenient for sample preparation through drop-casting of the solutions onto surfaces followed by solvent evaporation, the resulting particles or residues may not be representative of those in different explosives formulations. For example, formation of RDX α - and β -crystalline phases has been observed to depend on the amount of RDX deposited

from solutions onto surfaces, and different infrared spectral properties have been observed for the two phases.²⁶ The examples of explosives particles and residues in this manuscript are not intended to present a comprehensive study of particle size and sample preparation techniques for explosives detection; however, similar applications of the hyperspectral microscopy technique would be valuable for future systematic studies of the dependence of the infrared spectrum on particle morphology. For the examples presented in this manuscript, two sample preparation methods were used. To prepare tetryl and PETN residues, a $4 \mu\text{L}$ droplet of solution was deposited directly onto a ZnSe window, leaving behind a total mass of $4 \mu\text{g}$ when the solvent evaporated. To prepare RDX and PETN particles, solutions were placed in metal sample trays and evaporated, leaving behind crystals or particles of the explosives. Small particles were scraped from the sample trays and transferred to the ZnSe window for investigation in the hyperspectral microscope. No adhesive was used for attaching the explosives to the windows, as the electrostatic attraction was sufficient for the small particle sizes investigated.

3 Results

Figure 2(a) shows an image of particles of RDX obtained using the hyperspectral microscopy system, displayed as the mean transmitted intensity over all wavelength bands. The best image quality is obtained in the central portion of the image, with interference and diffraction effects becoming more noticeable near the edges. Each pixel in the image

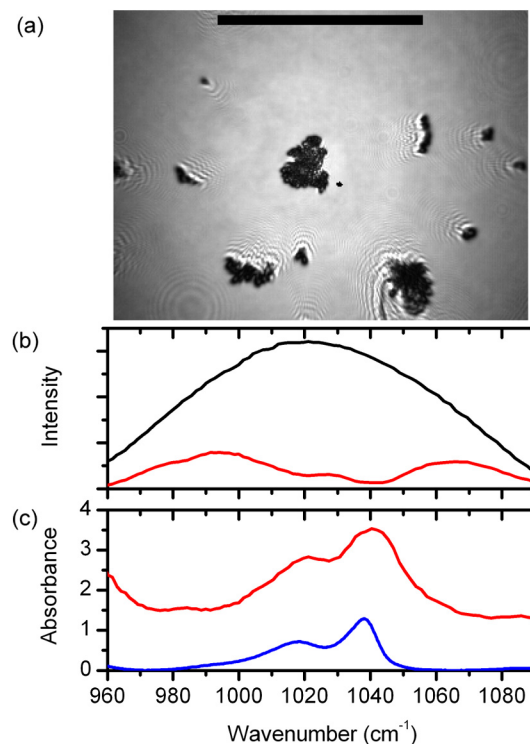


Fig. 2 Imaging of RDX particle. (a) Image of transmitted intensity, averaged over all spectral bands. The scale bar is 1 mm. (b) Spectra of transmitted light averaged over entire image (black, top trace) and averaged over a 5×5 pixel region in center of RDX particle (red, bottom trace). (c) Normalized absorbance spectrum of 5×5 pixel region in center of RDX particle (red, top trace) and reference spectrum for RDX obtained from FTIR film transmission (blue, bottom trace).

contains an associated transmission spectrum; Fig. 2(b) shows both the transmission spectrum averaged over all pixels in the image and over a 5×5 pixel region taken from the particle in the center of the image. The hyperspectral images were spectrally normalized by dividing the spectrum at each pixel by the mean spectrum over all pixels. This method was suitable for the low particle densities investigated here; for higher coverage samples the spectrum should be normalized to a user-selected portion of the image containing no sample, or to a separate blank image. However, normalizing to the mean transmission spectrum has the advantage of requiring no user input into the selection of a clean region of the image. An absorbance image A was calculated as $A = -\ln(T)$, where T is the normalized transmittance. Figure 2(c) shows an example of the normalized absorbance spectrum for the region in the RDX particle, and a comparison with a FTIR film transmission measurement taken on a different sample. While the peak locations and overall shape are similar between the two measurements, significant differences are also observed. For example, the microscopic spectrum presented here exhibits broadening of the absorption peaks, which may result from the high absorption for the thick particle. However, it is worth noting that the high spectral brightness of the ECQCL source allows transmission through thick particles with high absorption. A small peak shift is also observed, which may result from reflection losses at the particle surfaces contributing to the measured transmission spectrum.²⁷

The spectral information in each pixel can be used to highlight the chemical composition in the image. The top row in Fig. 3 shows a zoomed image of the RDX particle from Fig. 2. The lower row in Fig. 3 shows an image of a smaller RDX particle. A bicubic pixel interpolation was used in the zoomed images to smooth the image and reduce pixelation effects. Also note that the group of black pixels appearing in both images (and subsequent figures) is a damaged location on the FPA. Figure 3(a) shows the mean transmitted intensity for both RDX particles, showing the spatial structure of the particles. Figure 3(b) shows an image of the absorbance at 1040 cm^{-1} , corresponding to

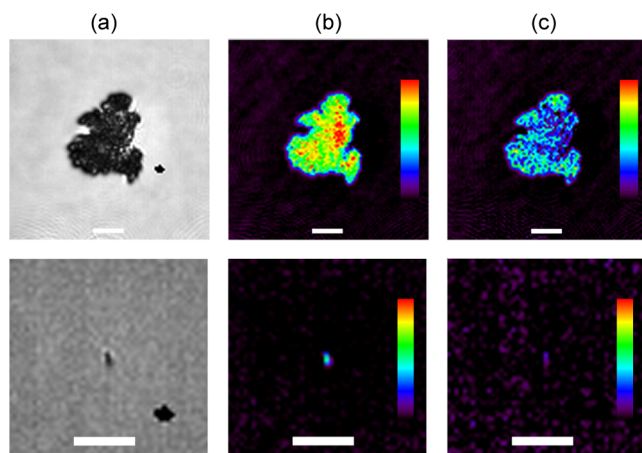


Fig. 3 Spectrally resolved images of large (top) and small (bottom) RDX particles. (a) Mean transmitted intensity over all spectral bands. (b) Absorbance image on-resonance of RDX absorption peak (1040 cm^{-1}). (c) Absorbance image off-resonance of RDX absorption peak (1075 cm^{-1}). The scale bar is $100 \mu\text{m}$, and the color ramp spans a range of absorbance values from 0–4.5.

a wavelength at the peak of the RDX absorption spectrum. A color mapping is used with red corresponding to high absorbance and black corresponding to low absorbance. Figure 3(c) shows an absorbance image at 1075 cm^{-1} , at a wavelength away from the RDX absorption peaks, and showing a smaller magnitude of absorption. Note that the particle is not completely transparent at this wavelength, in part due to nonresonant scattering and reflection effects. The small RDX particle shown in the lower row of Fig. 3 covers six pixels in the image, corresponding to an area of approximately $250 \mu\text{m}^2$. If we assume a spherical particle and an RDX density of 1.82 g/cm^3 , this particle has an approximate mass of 5 ng.

Figure 4(a) shows the mean transmission image for a collection of tetryl deposits on a window. The absorbance spectrum averaged over a group of nine pixels in the center of the large particle (indicated by the square in the image) is shown in Fig. 4(b) by the red curve; the blue curve shows an absorption spectrum obtained using FTIR spectroscopy on a different thin film of tetryl. As with the RDX particles, the peak locations and shape of the absorption spectrum of the tetryl particle obtained in the microscopy experiment match well with the reference FTIR measurements, with the exception of similar small peak shifts.

The spectral information associated with the image in Fig. 4(a) was used to locate a small tetryl particle barely visible in the mean transmission image. Figure 5(a) shows the absorbance spectrum obtained from a pixel near the center of the microscope image, in which the tetryl absorption peak at 1080 cm^{-1} is visible. Figure 5(b) shows a differential absorption image obtained by subtracting the peak absorbance at 1078.5 cm^{-1} from a two-point baseline defined by a straight line through the absorbance at 1064.2 and 1087.8 cm^{-1} . The color mapping reflects this differential absorption, and highlights the location of the particle. The particle covers two pixels, corresponding to approximate dimensions of $6 \times 12 \mu\text{m}$. Based on the measured particle

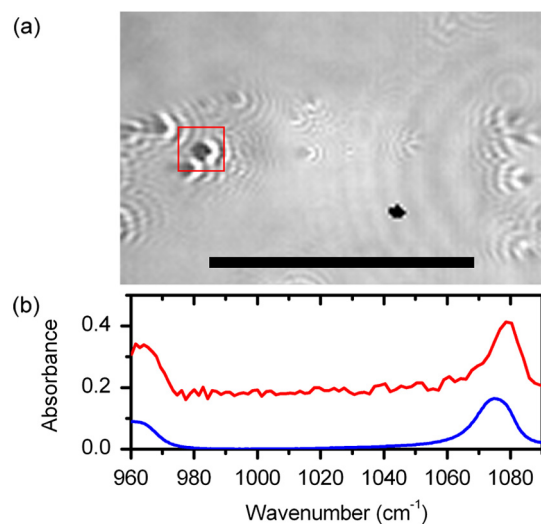


Fig. 4 Spectral imaging of tetryl residue. (a) Mean transmission averaged over all wavelengths. The scale bar is 1 mm. (b) Normalized absorbance spectrum of 3×3 pixel region in center of tetryl particle (red, top trace) and reference spectrum for tetryl obtained from FTIR film transmission (blue, bottom trace).

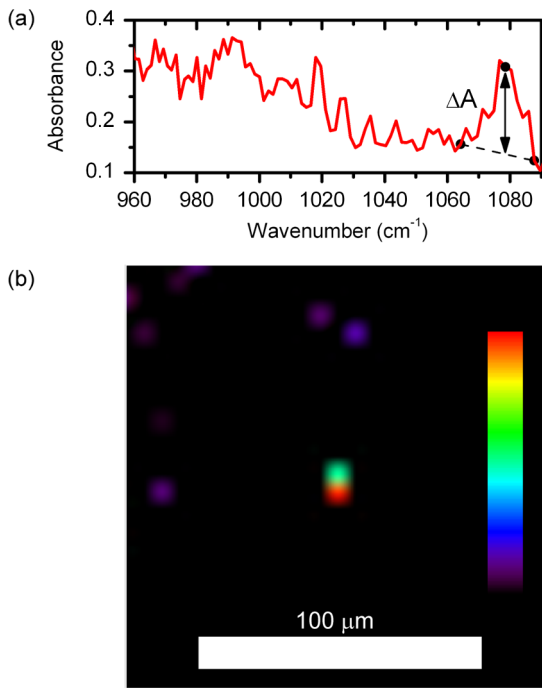


Fig. 5 (a) Absorbance spectrum of subnanogram tetryl particle. (b) Differential absorption image obtained by taking difference between peak and baseline of indicated tetryl peak. The scale bar is 100 μm and the color ramp spans absorbance values of 0.054 to 0.174.

size and a density of 1.73 g/cm^3 , the calculated mass for the tetryl particle is approximately 660 pg.

To demonstrate the potential of the hyperspectral infrared microscopy technique for material identification based on the infrared absorption spectrum, we performed a matched filter analysis as implemented in the ENVI software package.²⁸ The matched filter analysis determines the degree of similarity between an unknown spectrum and a set of library spectra (or endmembers), assigning a value between zero (no similarity) and one (identical spectra). Figure 6 shows library spectra used in the matched filter analysis, taken from normalized transmission spectra of particles of PETN, RDX, and tetryl in hyperspectral images. Hyperspectral images were selected for analysis which contained

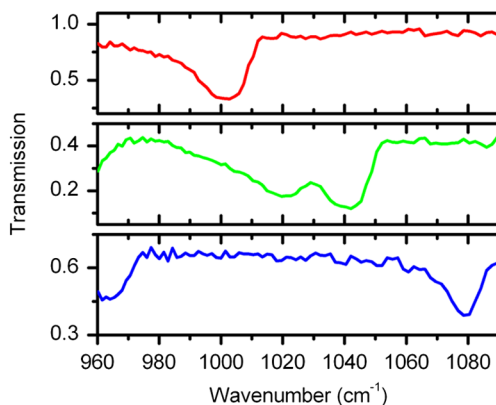


Fig. 6 Transmission spectra obtained from 9-pixel averages of particles identified in microscope images: PETN (red, top trace), RDX (green, middle trace), and tetryl (blue, bottom trace).

known particles of PETN, RDX, tetryl, and lint. Figure 7 shows the results of the matched filter analysis. The rows represent the different particles, while the columns show the results of the matched filter analysis at different thresholds of classification. The color coding in the image shows the results of the classification: red—PETN, green—RDX, and blue—tetryl. Column (i) shows the results at a low classification threshold of 0.1, which indicates a high degree of misclassification, or false positives, distributed across the images. Column (ii) shows a more useful classification threshold of 0.25, in which the number of false positives is greatly reduced. In particular, the lint particle shown in row (d) is not incorrectly identified as an explosive particle. Column (iii) shows results using a classification threshold of 0.5, which almost completely eliminates false positives in the identification, but at the expense of potentially missing some portions of particles or smaller particles, where the spectral match is not ideal. While not a comprehensive analysis, the matched filter results show one example of using the full spectral information to perform material identification, which could also be adapted for an automated detection algorithm.

The combination of spatial and spectral information can also reveal information about a sample unavailable when considering either factor alone. Figure 8 shows an example of hyperspectral imaging of a PETN residue. Figure 8(a) shows the mean transmission image, in which the PETN

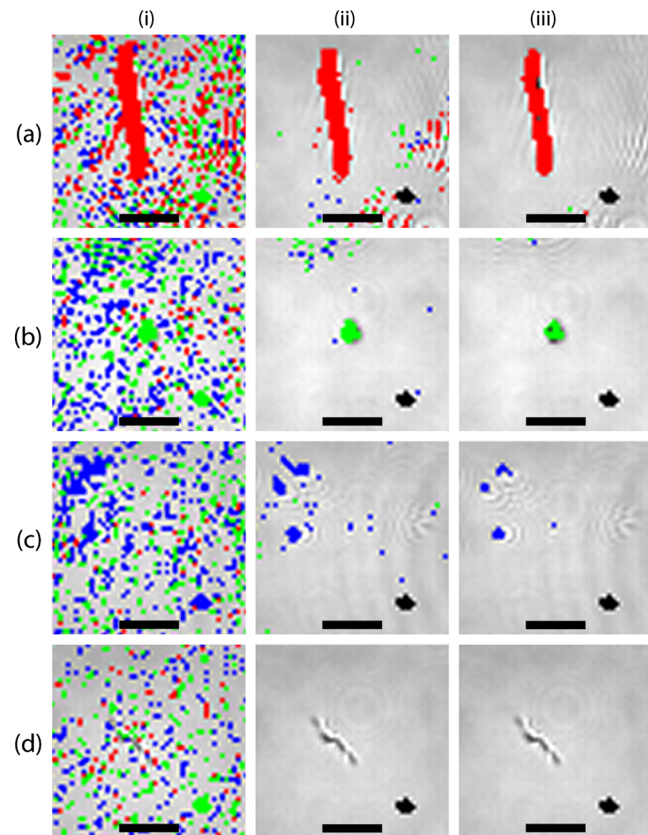


Fig. 7 Matched filter analysis of different materials. Each image shows the mean transmission in grayscale and is overlaid with the matched filter classification: PETN—red, RDX—green, tetryl—blue. The rows denote the materials (a) PETN, (b) RDX, (c) tetryl, and (d) lint. The columns show different thresholds for the matched filter classification (i) 0.10, (ii) 0.25, and (iii) 0.50. The scale bar is 100 μm .

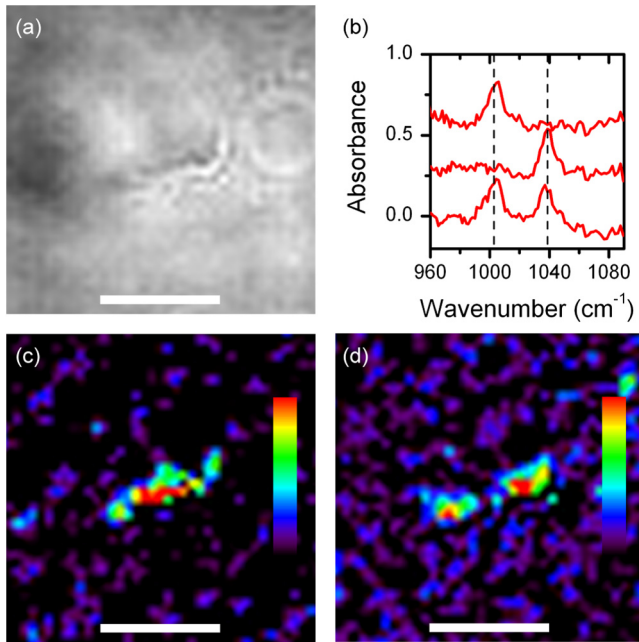


Fig. 8 Spectral imaging of PETN residue. (a) Mean transmission averaged over all wavelengths. (b) Normalized absorbance spectra from three selected pixels in PETN image. Curves have been offset for clarity. (c) Absorbance image at 1038.8 cm^{-1} . (d) Absorbance image at 1002.9 cm^{-1} . The scale bar is 100 μm and the color ramp spans absorbance values from 0 – 0.2.

residue is barely visible. Inspection of the hyperspectral image indicated that two absorption peaks were present, both the peak at 1000 cm^{-1} as observed for the PETN particles in Figs. 6 and 7, as well as an additional peak near 1040 cm^{-1} . Figure 8(b) shows absorption spectra taken from selected pixels in the image showing either the individual peaks or both peaks appearing simultaneously. Figure 8(c) and 8(d) shows absorbance images plotted for 1038.8 and 1002.9 cm^{-1} respectively. From the spectrally resolved images, it is apparent that the two absorption peaks correspond to different spatial locations within the PETN residue. It is worth noting that the ECQCL illumination was polarized along the horizontal axis of the image, which may be contributing to the two absorption resonances observed; however, additional polarization studies were not performed. While an investigation of the fundamental spectroscopy of PETN is not the focus of this paper, this example highlights the type of study made possible by the hyperspectral microscopy technique.

To characterize the noise performance and detection limits of the system, a hyperspectral image was collected of a blank scene containing nominally no absorbing particles. The image was normalized and the absorbance calculated for each pixel. The standard deviation of the spectrum at each pixel was then calculated as a measure of the spectral noise, and is plotted in Fig. 9(a). The absorbance noise is not uniform over the image, partly due to variation in the illumination power and partly due to interference and diffraction effects. In particular, a rectangular aperture is clearly visible near the edges of the image, likely due to the edges of the FPA. A small dust particle is also seen in the center of the image, where the higher absorbance noise results from a low laser power transmitted through the dust particle. A

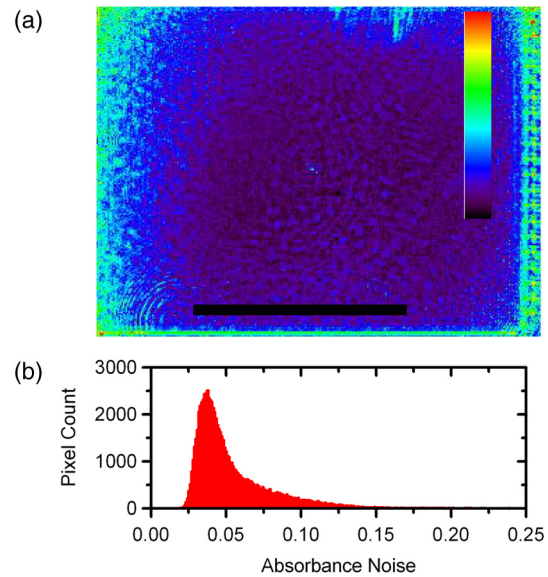


Fig. 9 Absorbance noise for nominally blank image. (a) Standard deviation of absorbance at each pixel. The scale bar is 1 mm and the color ramp spans absorbance values from 0 to 0.2. (b) Histogram of absorbance noise for all pixels.

histogram showing the distribution of absorbance noise for all pixels is shown in Fig. 9(b); the average absorbance noise over the entire image was determined to be 0.05.

The results presented above demonstrate the potential of the ECQCL-based hyperspectral microscopy technique for detection and identification of nanogram and subnanogram explosives particles. It is also interesting to calculate the expected detection limits based on physical and spectroscopic parameters, acknowledging that it is impossible to generalize to all materials and particle shapes. Solid materials typically have peak infrared absorption coefficients of 10^3 to 10^4 cm^{-1} . For example, in the spectral range probed by the ECQCL here, RDX has a peak absorption coefficient α of approximately 4000 cm^{-1} .²⁹ This corresponds to a minimum detectable thickness of 125 nm, expressed as a noise-equivalent value. A 10 μm thick particle should provide an absorbance of four, assuming a Beer's Law relationship of $A = \alpha L$ (although this not valid quantitatively for these high values of absorbance, it is used here for estimation purposes). Using the RDX density of 1.82 g/cm^3 , a 10 μm diameter spherical RDX particle has a mass of 715 pg. A particle of these dimensions should be resolvable by the microscopy imaging system, and also provide spectral absorption contrast with high SNR. It is worth noting that these calculations for estimated detection limits are somewhat conservative. In practice, it should be possible to detect the absorption from particles with dimensions smaller than a single pixel, even if the particle is not fully resolved in an imaging sense. In addition, using the full spectral information instead of the absorption at a single wavelength will further improve the SNR and detection limits.

4 Conclusions

We have presented a technique for performing hyperspectral microscopy using a broadly tunable ECQCL source to provide MIR illumination. Images were recorded with near

diffraction-limited performance at the infrared wavelengths used. The combination of a high-brightness ECQCL with a microbolometer FPA detector allows rapid data acquisition with high SNR. The apparatus was used to perform imaging of small explosives particles and residues, and a subnanogram detection limit was demonstrated. The spectral data contained in the hyperspectral images was used to measure absorption spectra of explosives on a microscale. This spectral data was used for material identification and characterization, and to highlight different features of an image unavailable by imaging with a single wavelength. An example of material identification was presented using a matched filter analysis. The noise of the system was characterized, and shows considerable room for improvement with optimization of imaging optics and reduction of coherent artifacts due to interference and diffraction. In addition, a multielement lens designed as a microscope objective could be used to improve image quality for off-axis points in the image. Development of broadband QC laser devices should allow for greater wavelength coverage from a single ECQCL system, and the compact size of the ECQCL allows for integration of multiple ECQCL sources.

Future work will adapt the microscopy apparatus to perform imaging in a reflection or scattering geometry, and will include investigation of other materials. The ability to detect and identify trace quantities of solid materials has direct applications in materials science, biology, forensics, and atmospheric sciences. In addition, continued study of the spectroscopy of explosives and other materials at a microscale will hopefully provide insight into standoff detection at greater distances, through correlation of spectroscopic properties with sample morphology. Although particles may not be spatially resolved individually in standoff detection applications, the microscopic spectroscopic properties are important in understanding the overall spectral response averaged over larger areas. For standoff detection of rough samples or residues, effects such as scattering from multiple particle interfaces are important and depend strongly on sample morphology.³⁰ Finally, development of reliable threat detection algorithms will require detailed knowledge of the expected spectral variations in explosives due to particle shape and size, crystalline form, sample matrix for mixed samples, background substrate effects, and observation geometry.

Acknowledgments

We thank Daylight Solutions for supplying the quantum cascade laser devices. The research described in this paper was conducted under the Laboratory Directed Research and Development Program at Pacific Northwest National Laboratory, a multiprogram national laboratory operated by Battelle for the U.S. Department of Energy under Contract DE-AC05-76RL01830.

References

- B. E. Bernacki and M. C. Phillips, "Standoff hyperspectral imaging of explosives residues using broadly tunable external cavity quantum cascade laser illumination," *Proc. SPIE* **7665**, 76650I (2010).
- M. C. Phillips and N. Ho, "Infrared hyperspectral imaging using a broadly tunable external cavity quantum cascade laser and microbolometer focal plane array," *Opt. Express* **16**(3), 1836–1845 (2008).
- M. C. Phillips, J. D. Suter, and B. E. Bernacki, "Hyperspectral microscopy using an external cavity quantum cascade laser and its applications for explosives detection," *Proc. SPIE* **8268**, 82681R (2012).
- I. W. Levin and R. Bhargava, "Fourier transform infrared vibrational spectroscopy imaging: integrating microscopy and molecular recognition," *Annu. Rev. Phys. Chem.* **56**, 429–474 (2005).
- E. N. Lewis et al., "Fourier-transform spectroscopic imaging using an infrared focal-plane array detector," *Anal. Chem.* **67**(19), 3377–3381 (1995).
- R. G. Messerschmidt and M. A. Harthcock, *Infrared Microspectroscopy. Theory and Applications*, Marcel Dekker, New York (1988).
- M. J. Nasse et al., "High-resolution Fourier-transform infrared chemical imaging with multiple synchrotron beams," *Nature Methods* **8**(5), 413–416 (2011).
- L. M. Miller and P. Dumas, "Chemical imaging of biological tissue with synchrotron infrared light," *Biochim. Biophys. Acta-Biomembr.* **1758**(7), 846–857 (2006).
- J. A. Reffner, P. A. Martoglio, and G. P. Williams, "Fourier-transform infrared microscopic analysis with synchrotron-radiation—the microscope optics and system performance," *Rev. Sci. Instrum.* **66**(2), 1298–1302 (1995).
- J. A. Bailey et al., "High spatial resolution for IR imaging using an IR diode laser," *Appl. Spectrosc.* **54**(2), 159–163 (2000).
- J. Faist et al., "Quantum cascade laser," *Science* **264**(5158), 553–556 (1994).
- B. Guo et al., "Multi-wavelength mid-infrared micro-spectral imaging using semiconductor lasers," *Appl. Spectrosc.* **57**(7), 811–822 (2003).
- A. Hugi, R. Maulini, and J. Faist, "External cavity quantum cascade laser," *Semicond. Sci. Technol.* **25**(8), 083001 (2010).
- F. Lu and M. A. Belkin, "Infrared absorption nano-spectroscopy using sample photoexpansion induced by tunable quantum cascade lasers," *Opt. Express* **19**(21), 19942–19947 (2011).
- M. Zhang et al., "Near-field spectroscopy of silicon dioxide thin films," *Phys. Rev. B* **85**(7), 075419 (2012).
- C. Bauer et al., "Potentials and limits of mid-infrared laser spectroscopy for the detection of explosives," *Appl. Phys. B: Lasers Opt.* **92**(3), 27–33 (2008).
- S. Wallin et al., "Laser-based standoff detection of explosives: a critical review," *Anal. Bioanal. Chem.* **395**(2), 259–274 (2009).
- F. Fuchs et al., "Imaging standoff detection of explosives using widely tunable midinfrared quantum cascade lasers," *Opt. Eng.* **49**(11), 111127 (2010).
- R. Furstenberg et al., "Stand-off detection of trace explosives via resonant infrared photothermal imaging," *Appl. Phys. Lett.* **93**(22), 224103 (2008).
- A. Mukherjee, S. Von der Porten, and C. K. N. Patel, "Standoff detection of explosive substances at distances of up to 150 m," *Appl. Opt.* **49**(11), 2072–2078 (2010).
- C. W. Van Neste, L. R. Senesac, and T. Thundat, "Standoff photoacoustic spectroscopy," *Appl. Phys. Lett.* **92**(23), 234102 (2008).
- M. C. Phillips et al., "Challenges of infrared reflective spectroscopy of solid-phase explosives and chemicals on surfaces," *Proc. SPIE* **8358**, 83580T (2012).
- J. R. Verkouteren, "Particle characteristics of trace high explosives: RDX and PETN," *J. Forens. Sci.* **52**(2), 335–340 (2007).
- M. C. Phillips et al., "Design and performance of a sensor system for detection of multiple chemicals using an external cavity quantum cascade laser," *Proc. SPIE* **7608**, 76080D (2010).
- S. W. Sharpe et al., "Gas-phase databases for quantitative infrared spectroscopy," *Appl. Spectrosc.* **58**(12), 1452–1461 (2004).
- P. Torres et al., "Vibrational spectroscopy study of β and α RDX deposits," *J. Phys. Chem. B.* **108**(26), 8799–8805 (2004).
- P. Bassan et al., "Reflection contributions to the dispersion artefact in FTIR spectra of single biological cells," *Analyst* **134**(6), 1171–1175 (2009).
- ITT Visual Information Systems, <http://www.itvis.com>.
- R. A. Isbell and M. Q. Brewster, "Optical properties of energetic materials: RDX, HMX, AP, NC/NG, and HTPB," *Propellants Explos. Pyrotech.* **23**(4), 218–224 (1998).
- J. Suter, B. Bernacki, and M. Phillips, "Spectral and angular dependence of mid-infrared diffuse scattering from explosives residues for standoff detection using external cavity quantum cascade lasers," *Appl. Phys. B: Lasers Opt.* **108**(4), 965–974 (2012).

Mark C. Phillips is a senior research scientist specializing in laser spectroscopy at Pacific Northwest National Laboratory in Richland, Washington. He joined Pacific Northwest National Laboratory in 2005 to perform research and development of mid-infrared technology based on quantum cascade lasers. He has worked to develop external cavity quantum cascade laser systems and sensors for trace gas detection and hyperspectral imaging. He was employed as a postdoctoral fellow at Sandia National Laboratory from 2002 to 2005, and researched quantum coherence effects in semiconductor quantum dots. He received his PhD from University of Oregon in 2002 where he studied fundamental quantum optics in semiconductor nanostructures. He is a member of the Optical Society of America.

Bruce E. Bernacki has worked at Pacific Northwest National Laboratory, a DOE Office of Science laboratory managed by Battelle Memorial Institute, since 2005 as a senior research scientist. An optics professional with 25 years of experience in optical design, modeling, optical component manufacturing, and optical data storage, he holds PhD and MS degrees in Optical Sciences, as well as a BSEE, all from the University of Arizona. He has worked in both the

government and private sector in both basic research and product development environments. At PNNL his research activities include optical design for applications ranging from the UV to submillimeter wave region, waveguide design and analysis, stray light analysis, physical optics modeling, thin film design and optical instrument design and fabrication for various spectroscopic, imaging and fluorescence methods.